Chemical
Science

ROYAL SOCIETY
OF CHEMISTRY

EDGE ARTICLE

View Article Online
View Journal | View Issue

Check for updates

Cite this: *Chem. Sci.*, 2026, **17**, 3593

All publication charges for this article have been paid for by the Royal Society of Chemistry

Received 16th August 2025
Accepted 19th December 2025

DOI: 10.1039/d5sc06257h

rsc.li/chemical-science

Pd–Cu dual-site tuned H adsorption for efficient electrocatalytic hydrogenation of HMF

Guozhou Feng, Yuxin Fan, Lechen Diao, * Zhichao Miao and Jin Zhou *

Electrocatalytic hydrogenation (ECH) of 5-hydroxymethylfurfural (HMF) to 2,5-bis(hydroxymethyl)furan (BHMF) is regarded as a green synthesis strategy for generating high quality bio-based chemicals. However, simultaneously regulating both the hydrogen (H) coverage and the adsorption behavior of HMF presents a significant challenge, particularly in unraveling the intricate structure–activity relationship and achieving a selective target product. Here, we enhance the availability of hydrogen (H*) and modulate surface electronic interactions with 5-hydroxymethylfurfural (HMF) to facilitate selective electrochemical hydrogenation (ECH) of HMF by introducing palladium as an auxiliary component. Pd–Cu dual sites synergistically enhanced H* supply and HMF activation while suppressing the competing hydrogen evolution reaction. The optimized electrocatalyst exhibits notable catalytic performance, attaining a selectivity of 99.3% and a faradaic efficiency of 97.5% for BHMF at a potential of −1.15 V (*vs.* Ag/AgCl). Density functional theory (DFT) calculations demonstrate that Pd doping is crucial for enhancing the adsorption of H* and HMF* intermediates, thereby promoting the hydrogenation of HMF through the Langmuir–Hinshelwood (L–H) mechanism under neutral conditions. This work establishes a catalyst design paradigm where atomic-level dopant engineering regulates multistep protonation kinetics, offering fundamental insights into biomass electrorefining.

Introduction

With the depletion of traditional fossil resources and increasing demand for fine chemicals and polyester materials, the conversion of biomass into platform chemicals is getting increasing attention due to their relevance in sustainable development. Featuring both hydroxyl and aldehyde functional groups, HMF serves as a versatile precursor that can be transformed into high-value derivatives through selective chemical modifications.[1–7] The directional catalytic reduction of the aldehyde group of HMF yields 2,5-bis(hydroxymethyl)furan (BHMF), a dihydroxy-containing compound, which serves as a key precursor for pharmaceutical intermediates and advanced polymer materials.[8,9] Current industrial processes predominantly employ conventional thermal catalysis for HMF hydrogenation under high-pressure H_2 and elevated temperature conditions, which is accompanied by excessive hydrogenolysis and hydrogenation of the furan ring.[10,11] This has driven research interest in developing alternative hydrogenation methods that operate under milder conditions without gaseous H_2. Electrochemical hydrogenation is considered a promising approach, utilizing H from H_2O under ambient conditions, thereby eliminating the need for external H_2 supply.[12,13] This green and eco-friendly synthesis strategy enables selective production of BHMF through direct electron transfer processes, aligning with sustainable energy utilization principles.[14] What's more, the electrocatalytic hydrogenation reaction can achieve better target product selectivity by controlling the catalyst and potential.[15]

The prevailing mechanism for electrochemical hydrogenation of HMF is the L–H mechanism, which involves water splitting to produce H adsorbed on the electrode surface (denoted as H*), followed by the reaction of H* with HMF* to produce BHMF.[16–18] Mostly, Cu-based catalysts exhibit inferior activity for the electrocatalytic hydrogen evolution reaction (HER) while exhibiting superior selectivity for hydrogenation due to their abundant d-orbital electrons, which are regarded as potential catalysts for the efficient electrosynthesis of BHMF.[19,20] Nevertheless, studies find that pure Cu species struggle to balance HMF activation and H* supply capability simultaneously. As a result, the intermediate products (HMF*) generated from electrochemical adsorption are not hydrogenated promptly, leading to HMF dimerization. To address this challenge, researchers have developed various Cu-based catalysts, including Ga-doped Ag–Cu,[21] PMo_{12}/Cu,[22] RhCu,[23] Cu/MOx Cu,[24] and CuFeOx/CF,[25] all demonstrating enhanced HMF hydrogenation performance in aqueous media under mild conditions. These designs primarily aim to optimize the balance between HMF adsorption and H* availability through synergistic effects from secondary components. While increased H* surface coverage proves critical for efficient

---

School of Chemistry and Chemical Engineering, Shandong University of Technology, Zibo 255000, PR China. E-mail: diaolechen@sdut.edu.cn; zhoujin@sdut.edu.cn

hydrogenation, a paradoxical competition emerges: excessive H* tends to recombine into H_2 gas, significantly reducing the faradaic efficiency toward BHMF production.[21] This fundamental trade-off highlights the necessity for precision engineering of catalysts. Therefore, introducing suitable proton supplying sites might provide H* with appropriate protonation capability, which facilitates efficient and selective hydrogenation of HMF to BHMF.

Pd is a group VIII element known for its strong O–H activation and proton affinity. Among transition metals, it is located at the top and center-left of the hydrogen evolution reaction (HER) volcano plot, highlighting its potential as an ideal element to generate sufficient *H without causing excessive HER. In addition, Pd-based materials were usually used to activate HMF.[26,27] Therefore, introducing Pd atoms into Cu-based catalysts may balance H* supply ability and HMF adsorption behavior of the catalysts, significantly improving their electrocatalytic HMF hydrogenation performance.

Herein, we report a rationally designed Pd–Cu heterostructure catalyst supported on three-dimensional carbon matrices (denoted as *x*%Pd-Cu@3DC, where *x* indicates Pd molar fractions) for electrochemical conversion of HMF to BHMF. The optimized 3%Pd-Cu@3DC electrocatalyst demonstrates exceptional performance metrics at an applied potential of −1.45 V (*versus* Ag/AgCl), achieving 97% HMF conversion efficiency, 99.3% BHMF selectivity, and 97.5% faradaic efficiency, substantially outperforming monometallic Cu catalysts and other Cu-based catalysts. Mechanistic analysis reveals two interdependent functions facilitated by atomic-level Pd incorporation. On one hand, Pd sites synergistically promote water splitting to generate reactive hydrogen species (H*), enabling rapid hydrogenation of the critical $C_6H_7O_3$* intermediate. On the other hand, the interaction between Cu and Pd atoms could also modulate the electronic structure of the catalyst, which enhances the adsorption of HMF and the selective protonation of *CHO.[28] This catalyst design strategy certifies that suitable proton-supplying sites can effectively regulate multiple protonation steps to facilitate the conversion of HMF to BHMF.

Results and discussion

Catalyst synthesis and characterization

The Pd-Cu@3DC catalysts were fabricated through a modified lyophilization–calcination synthesis strategy (Fig. 1a).[29] Initially, a homogeneous precursor solution was prepared by dissolving $PdCl_2$, $Cu(NO_3)_2$, glucose, and NaCl in deionized water. This solution subsequently underwent freeze-drying at −20 °C for 20 h, followed by thermal annealing at 700 °C for 2 h under an H_2/Ar atmosphere. The resulting carbonaceous composite was then subjected to thorough aqueous washing to eliminate NaCl templates, ultimately yielding hierarchically porous honeycomb architectures with atomic-level Pd–Cu coordination nanoparticles.

Microstructural characterization reveals critical morphological features of the Pd-Cu@3DC catalyst. Scanning electron microscopy (SEM) and transmission electron microscopy (TEM) analyses (Fig. S1 and Fig. 1b) demonstrate the formation of three-dimensionally interconnected ultrathin carbon skeletons with hierarchical porosity, establishing continuous conductive pathways for efficient electron transfer and electrolyte infiltration. Through a spherical Aberration Corrected Transmission Electron Microscope (AC-STEM) in Fig. 1c, distinct isolated bright spots were identified. We measured the interplanar spacing and found that it increased by 0.02 nm compared with that of the (200) plane in the standard Cu reference card (0.181 nm). The presence of a single Pd atom within a column of Cu atoms indicates that the Pd atom exists in a single-atom form. Energy-dispersive spectroscopy (EDS) mapping images (Fig. 1d) showed that the distribution contours of Cu and Pd elements highly overlapped with the STEM images, suggesting partial substitution of Cu atoms by Pd. Crystallographic analysis of the Pd-Cu@3DC catalysts was performed through X-ray diffraction (XRD) patterns. The XRD patterns (Fig. S2a) display characteristic diffraction peaks at 43.3°, 50.4°, 74.1°, and 89.9°, indexed to the (111), (200), (220), and (311) planes of face-centered cubic (fcc) Cu (JCPDS 04-0836). Additional reflections at 35°, 36.4°, 37°, and 62° are in good agreement with the peaks of monoclinic CuO (JCPDS 44-0706), and the peak at 36.4° corresponds to Cu_2O (JCPDS 05-0667), which arises from surface oxidation during ambient exposure. Notably, substituting smaller ions with larger counterparts induces lattice expansion, which in turn increases the interplanar spacing *d*. As dictated by Bragg's law ($n\lambda = 2d\sin\theta$), with a fixed X-ray wavelength (λ), an increase in *d* inevitably leads to a decrease in $\sin\theta$. This phenomenon consequently results in a shift of the diffraction angle (θ) toward lower values. All Cu-related peaks exhibit a systematic negative shift of 0.15–0.23° compared to pristine Cu@3DC (Fig. 1e), indicative of lattice expansion caused by partial substitution of smaller Cu atoms ($r = 0.128$ nm) with larger Pd atoms ($r = 0.137$ nm). This, together with the AC-STEM results, indicates that Pd is incorporated into the catalyst as single atoms. Fig. S2b shows the Raman spectra of 3%Pd-Cu@3DC, where two prominent peaks appear at 1350 and 1580 cm^{-1}, corresponding to the D peak (amorphous carbon) and G peak (crystalline graphite), respectively. The peak intensity ratio (I_D/I_G) of 3%Pd-Cu@3DC is about 0.14, reflecting that the high graphitization degree of the samples is due to the catalytic role of Cu. As shown in Fig. S13, the XRD patterns of 3%Pd-Cu@3DC before and after reduction reveal that the characteristic diffraction peaks corresponding to CuO and Cu_2O have vanished. Given that the catalyst was supported on carbon paper for XRD measurements, several extra characteristic diffraction peaks of carbon paper are detected in comparison with other XRD patterns.

X-ray photoelectron spectroscopy (XPS) characterization was performed to identify the chemical valence states of the Pd-Cu@3DC catalysts. As shown in Fig. 1f and g, the characteristic peaks of Cu 2p and Pd 3d are located at the same position in the four samples. The Cu 2p high-resolution XPS spectra can be divided into four subpeaks, representing Cu^0/Cu^+ species ($2p_{3/2}$, 933.8 eV; $2p_{1/2}$, 954.4 eV) and Cu^{2+} species ($2p_{3/2}$, 935.7 eV; $2p_{1/2}$, 955.8 eV), respectively. Notably, Cu atoms show a slight surface oxidation in the Pd-Cu@3DC. With the increasing Pd doping, the valence state of Cu atoms transforms from +2 valence to +1/0 valence. Moreover, the Pd 3d XPS spectra of Pd-Cu@3DC

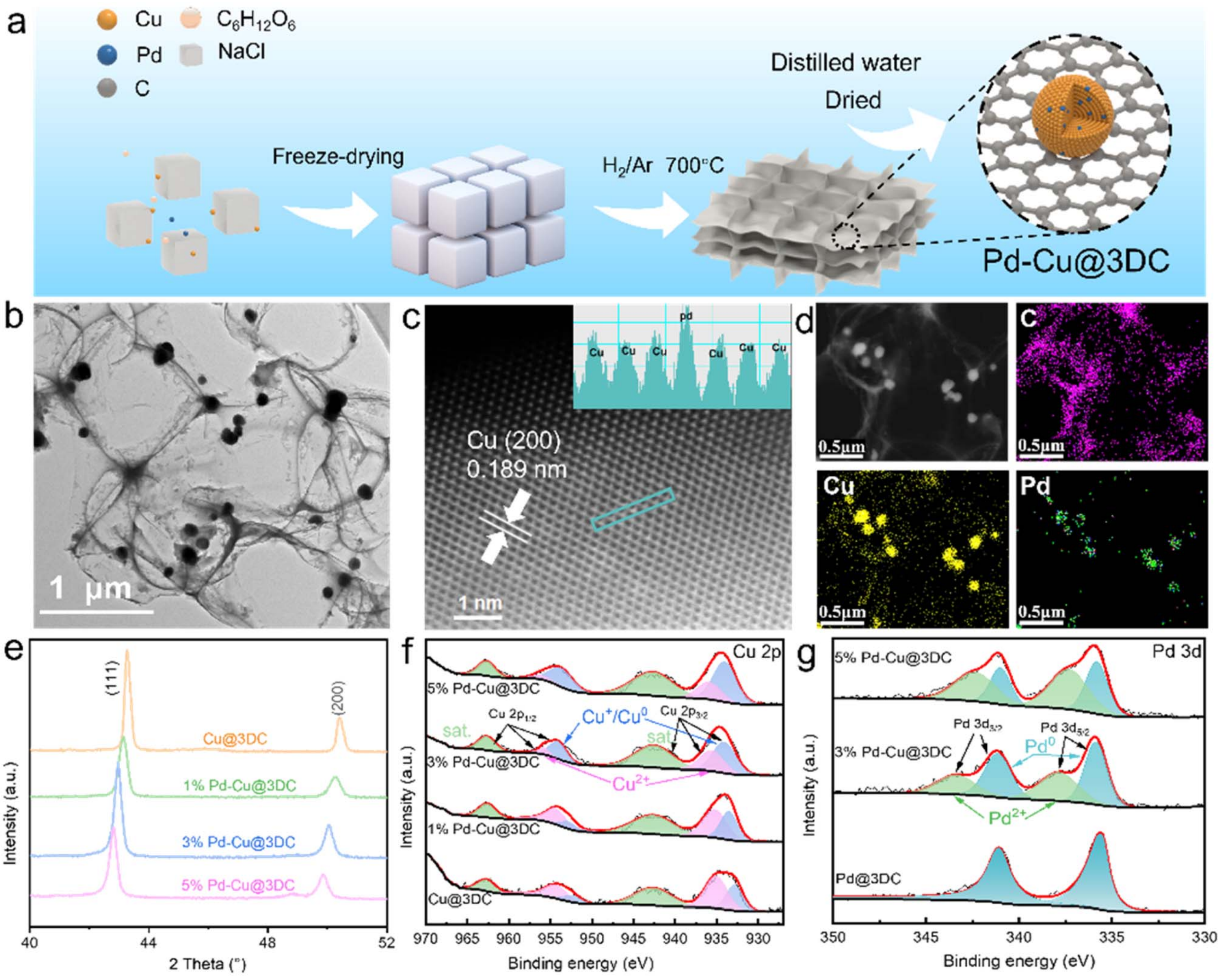

Fig. 1 Synthetic routes and structural characterization for Pd-Cu@3DC. (a) Illustration of the synthetic routes. (b) TEM image and (c) AC-STEM image. (d) EDS mapping images of 3%Pd-Cu@3DC. (e) XRD patterns of 3%Pd-Cu@3DC. High-resolution XPS spectra of (f) Cu 2p and (g) Pd 3d of 3%Pd-Cu@3DC.

exhibit an obvious oxidized state compared to monometallic Pd@3DC. These results indicate the successful incorporation of Pd into the Cu nanoparticles and electron transformation from Pd to Cu within the alloy structure.

Electrocatalytic hydrogenation performance

Before assessing the catalytic performance of Pd-Cu@3DC towards HMF hydrogenation, the CuO and Cu_2O on the surface of Pd–Cu nanoparticles were first reduced into metal by the galvanostatic method. Then, the linear sweep voltammetry (LSV) curves were recorded in 0.5 M $KHCO_3$ solution (pH∼8.17) with or without adding 50 mM HMF. As shown in Fig. 2a and b, incorporation of the Pd atom into Cu significantly reduces the overpotential of the HER. Moreover, the presence of HMF further decreases the overpotential of the reaction process, which indicates that Pd-Cu@3DC is active in the electrocatalytic HMF hydrogenation. The catalytic kinetic curves of the catalyst for the HER and HMF hydrogenation are shown in Fig. 2c as Tafel plots derived from polarization curves.[30] The Tafel slopes of Cu@3DC and 3%Pd-Cu@3DC for the HER were 271.99 and 504.52 mV dec^{-1}, respectively, illustrating that the Volmer step dominates the HER rate.[31] Meanwhile, as demonstrated by the attenuated total reflection surface-enhanced infrared absorption spectroscopy (ATR-SEIRAS) spectra in Fig. S12a and b, the complete absence of the adsorbed hydroxyl (OH*) stretching band at 3256 cm^{-1} provides definitive evidence that H* is generated *via* the Volmer step ($H_2O + e^- \rightarrow H^* + OH^-$), with the generated OH^- transferring to the electrolyte solution.[32] For the HMF hydrogenation reaction, the Tafel slopes of Cu@3DC and 3%Pd-Cu@3DC were measured to be 302.05 and 132.97 mV dec^{-1}, respectively. Both values are lower than those obtained by the HER. These results suggest that the HMF hydrogenation process holds a greater advantage over the HER process.

The electrocatalytic hydrogenation performance was systematically evaluated through chronoamperometric analyses in 50 mM HMF electrolyte, with reaction products quantified *via* HPLC (Fig. 2d and S3). Fig. 2e and S4 compare the potential-

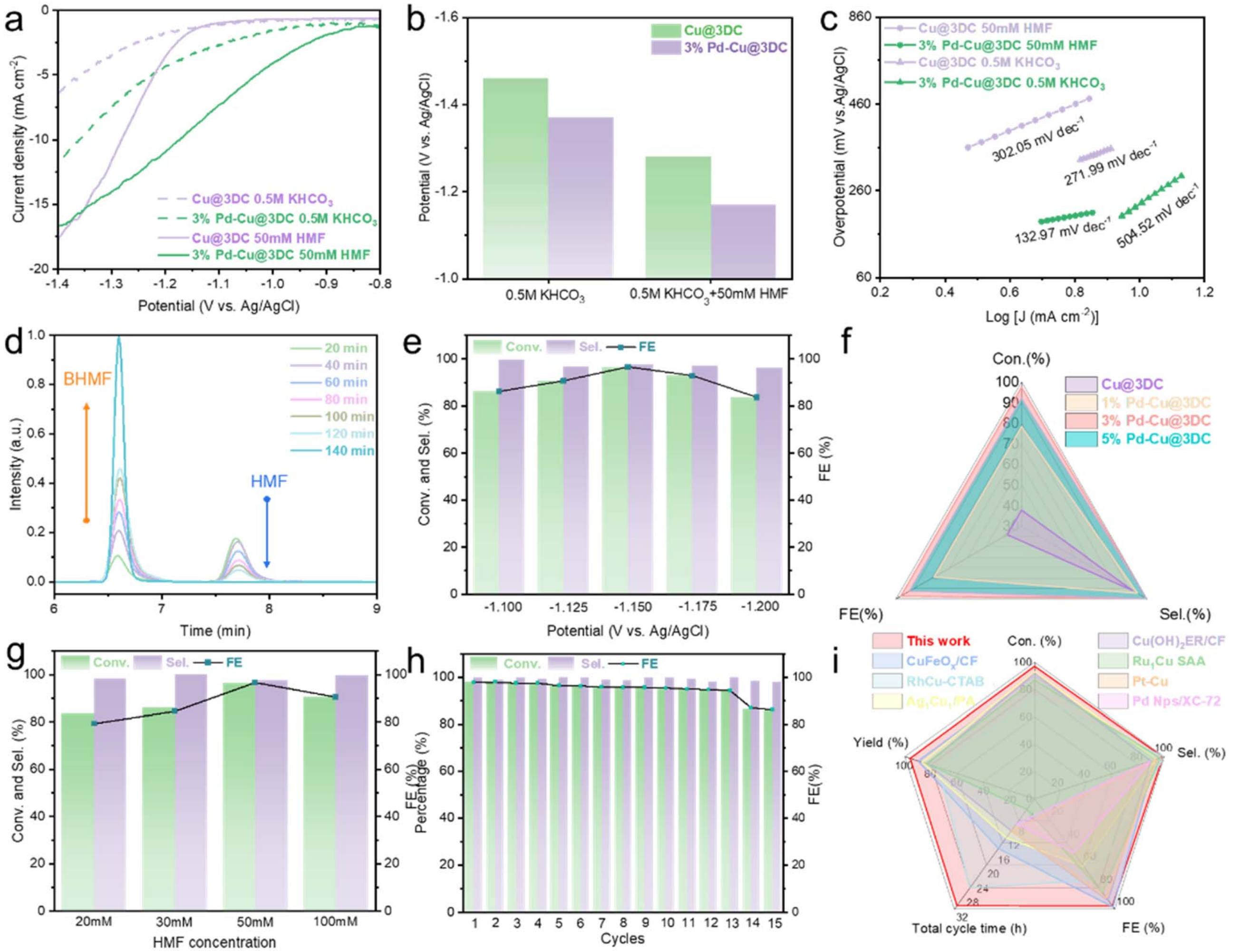

Fig. 2 Electrochemical performance of the catalysts. (a) LSV curves, (b) potential comparison (at 10 mA cm^{-2}) and (c) Tafel slopes of Cu@3DC and 3%Pd-Cu@3DC in 0.5 M $KHCO_3$ solution with and without 50 mM HMF. (d) HPLC chromatograms of the electrolyte at different electrolysis times. (e) Potential screening of chronoamperometric electrolysis of HMF on 3%Pd-Cu@3DC. (f) Performance comparison of different Pd-Cu@3DC catalysts. (g) Catalysis performance of 3%Pd-Cu@3DC at different HMF concentrations. (h) Cycling electrolysis stability of 3%Pd-Cu@3DC. (i) Performance comparison with the literature (data obtained from Table S1).

dependent activity profiles of Cu@3DC and Pd-Cu@3DC catalysts. The monometallic Cu@3DC catalyst exhibits limited conversion efficiency (<25%) and faradaic efficiency (FE < 30%) across the tested potential window (−1.1 to −1.3 V *vs.* Ag/AgCl), despite retaining 95–98% BHMF selectivity. The 3%Pd-Cu@3DC catalyst demonstrates superior catalytic performance. As the potential increased, the efficiency of H* generation improved. As a result, the catalytic performance gradually improved. When the potential reached −1.15 V (*vs.* Ag/AgCl), 3%Pd-Cu@3DC achieves near-complete (97%) conversion efficiency, 97.5% FE, and 99.3% BHMF selectivity, outperforming Cu@3DC under identical conditions. Further increases in the potential lead to a decline in HMF conversion and FE due to intense competition from the HER. A multivariate radar chart (Fig. 2f and S4) highlights the tripartite performance superiority (conversion, selectivity, and FE) of 3%Pd-Cu@3DC over other Pd-Cu@3DC catalysts, establishing its optimal catalytic functionality. To gain deeper insights into the origin of the electrode performance for HMF hydrogenation, the electrochemical active surface area (ECSA) was evaluated based on the double-layer capacitance (C_{dl}) at different scan rates (Fig. S11). Compared with Cu@3DC (2.4 mF cm^{-2}), the C_{dl} of 3% Pd-Cu@3DC (13.2 mF cm^{-2}) is significantly increased, exhibiting more accessible active sites for HMF adsorption. To accurately evaluate the intrinsic catalytic capability of the synthesized materials, the electrochemical performance was normalized by the ECSA, considering that the apparent activity could be affected by the difference in the ECSA. As shown in Fig. S11d, the normalized current density of 3%Pd-Cu@3DC reaches −0.0042 mA cm_{ECSA}^{-2} at −1.15 V (*vs.* Ag/AgCl), which is 1.5 times that of Cu@3DC, indicating the enhanced intrinsic catalytic activity induced by Pd doping.

In addition to the potential, the influence of concentrations on conversion and FE was also evaluated, as shown in Fig. 2g. Concentration-dependent studies reveal a positive correlation between HMF concentration (20–50 mM) and ECH efficiency for 3%Pd-Cu@3DC, with maximum values reaching 97% conversion and 97.5% FE at 50 mM HMF. This enhancement stems from suppressed hydrogen evolution reaction (HER) kinetics at elevated substrate concentrations, where competitive HMF adsorption dominates active sites. Notably, 3%Pd-Cu@3DC exhibits exceptional operational stability, preserving 99.1% BHMF selectivity even at 100 mM HMF, though with moderate efficiency declines (conversion: 94.2%, FE: 92.5%). These reductions arise from mass transport limitations and insufficient H* under high substrate concentrations. Interestingly, bis(hydroxymethyl)hydrofuroin (BHH) was not observed throughout the entire reaction process, which is different from previous reports. According to previous reports, if the catalyst interacts with the HMF through the oxygen coordination configuration, it prefers to promote the two-electron production of $-CH_2OH$ *via* an $R-CH_2-O^*$ intermediate.[33,34]

Long-term stability is critical for electrocatalysts intended for industrial applications. Consecutive chronoamperometric electrolysis was performed to evaluate the stability of the 3%Pd-Cu@3DC catalyst. As shown in Fig. 2h, the 3%Pd-Cu@3DC catalyst displays robust performance throughout 13 successive electrolysis experiments. The HMF conversion and FE remain consistently above 95% during all cycles, suggesting the excellent stability of 3%Pd-Cu@3DC. In comparison with analogous reports in the literature, the 3%Pd-Cu@3DC catalyst exhibits outstanding hydrogenation performance for HMF (Fig. 2i and Table S1).

Reaction kinetics analysis

Kinetic experiments were conducted to get insights into the reaction process for the electrochemical hydrogenation of HMF over Cu@3DC and 3%Pd-Cu@3DC. We tracked the concentration, selectivity, and FE of BHMF during HMF electrochemical hydrogenation. As presented in Fig. 3a, HMF was gradually consumed in the electrolyte, while BHMF quickly increased with the reaction proceeding. Correspondingly, selectivity and FE remain up to 95% during the electroreduction process. On account of these experimental results, a simplified reaction model was developed to investigate the kinetics of the electrochemical hydrogenation of HMF over Cu@3DC and 3%Pd-Cu@3DC (Fig. 3b and S5).[35] The kinetic behavior was hypothesized to be the pseudo-first order reaction for this reaction step in which the H_2O concentration was constant, and the kinetic equation can be seen in Fig. 3b. Notably, after the introduction of Pd atoms, the reaction rate constant (k) of 3%Pd-Cu@3DC significantly increased compared with that of Cu@3DC, indicating that the Pd dopant could promote the electrochemical hydrogenation reaction. To better comprehend catalytic reactions, it is crucial to determine the apparent activation energy (E_a). Then, Arrhenius plots derived from k estimated at three different temperatures (20–60 °C) are shown in Fig. 3c and S6c. All curves were fitted with a correlation coefficient above 0.99, suggesting a good linear correlation.[36] E_a values were obtained from the slope of the Arrhenius plots, while the pre-exponential frequency factor corresponds to the intercept. Obviously, the E_a for Cu@3DC is 2.1 kJ mol^{-1}, while the E_a for 3%Pd-Cu@3DC significantly decreased down to 1.45 kJ mol^{-1}. The lower energy barrier is beneficial for accelerating the reaction.

Charge transfer kinetics at the electrode interface plays a crucial role in electrocatalytic reactions. Nyquist and Bode plots were further collected through *operando* electrochemical

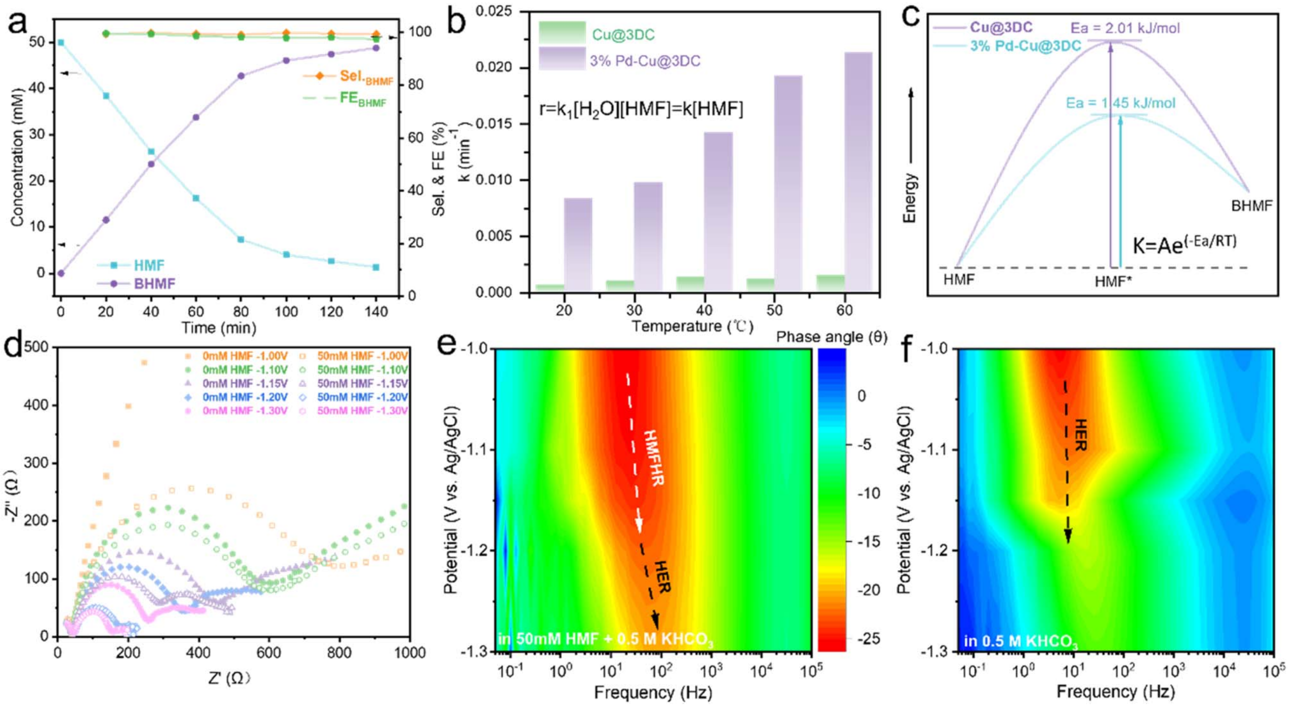

Fig. 3 Reaction kinetic analysis of the ECH. (a) HPLC quantitative results at −1.15 V *vs.* Ag/AgCl on 3%Pd-Cu@3DC. (b) Reaction rate constant k at reaction temperature from 20–60 °C on 3%Pd-Cu@3DC and Cu@3DC. (c) E_a of electrochemical HMF hydrogenation on 3%Pd-Cu@3DC and Cu@3DC. (d–f) EIS characterization of 3%Pd-Cu@3DC and (d) Nyquist and (e and f) Bode plots.

impedance spectroscopy (EIS) within the potential window of 1.0–1.3 V. As displayed in Fig. 3d, the semicircles of 3%Pd-Cu@3DC catalyzed HMF electrochemical hydrogenation are notably smaller than those of the blank group without HMF under the same operating conditions, indicating that HMF addition has reduced the resistance at the reaction interface. This trend is more apparent for 3%Pd-Cu@3DC than Cu@3DC, as shown in Fig. S6a. Subsequently, the charge transfer behaviors were investigated using the Bode plots (Fig. 3e and f). The peak of the blank group in the low frequency region corresponds to the Volmer step. Owing to the slow kinetics of the Tafel step and Heyrovsky step at low potentials, the H* on the surface of the catalyst hardly generates H_2 and the Volmer step easily achieves dynamic equilibrium, which leads to no electron transfer occurring on the reaction interface. After introducing the HMF, the peak intensity weakens significantly and the peak position shifts to a higher frequency, attributed to the consumption of H* by the aldehyde groups in the HMF, which breaks the dynamic equilibrium of the Volmer step and the HMF hydrogenation step predominates the next reaction.[37] When the potential increases to 1.2 V, the peaks of both blank and experimental groups shift to a higher frequency, showing less difference between the two peaks. This is attributed to the HER, which predominates the main reaction at high operation potential.

Electrocatalytic reaction mechanism

As the H* availability plays a vital role in determining the kinetics of HMF hydrogenation, especially for its selectivity and FE, cyclic voltammetry (CV) tests were carried out in $KHCO_3$ electrolyte to investigate the H* coverage on the catalyst surface. As shown in Fig. 4a, the curves show a pair of redox peaks in the anodic scan for 3%Pd-Cu@3DC, which correspond to H* adsorption and desorption.[38] 3%Pd-Cu@3DC exhibits an apparent H* desorption peak, indicating the existence of a large amount of H* on the surface of the electrode, which will lead to additional HER and lower FE. After the addition of HMF, the desorption peaks of H* became smaller and were completely suppressed in both samples at 20 mM HMF. Meanwhile, the adsorption peaks shift towards positive potential, implying that HMF adsorption occurred prior to H* adsorption, which may occupy the sites of H*. Thus, the decreased H* adsorption can be attributed to the consumption by HMF reduction and the HMF adsorption.[39]

The local pH evolution during HMF electrochemical hydrogenation was quantitatively monitored using a rotating ring-disk electrode (RRDE) system through ring open-circuit potential (OCP) measurements (Fig. 4b).[40,41] A calibration curve was first established by correlating OCP (*vs.* Ag/AgCl) with bulk electrolyte pH, which coincides with the Nernst equation in response to the change in pH (Fig. S7). RRDE analysis revealed significant interfacial pH variations between 3%Pd-Cu@3DC and Cu@3DC catalysts. For 3%Pd-Cu@3DC, the electrode–electrolyte interface pH increased from 8.9 to 9.4 as the applied potential shifted from −1.1 V to −1.2 V *vs.* Ag/AgCl, indicative of rapid formation of reactive hydrogen species (H*) and OH^- through splitting of H_2O. In contrast, the pH values of the Cu@3DC surface are much lower than those of 3%Pd-Cu@3DC,

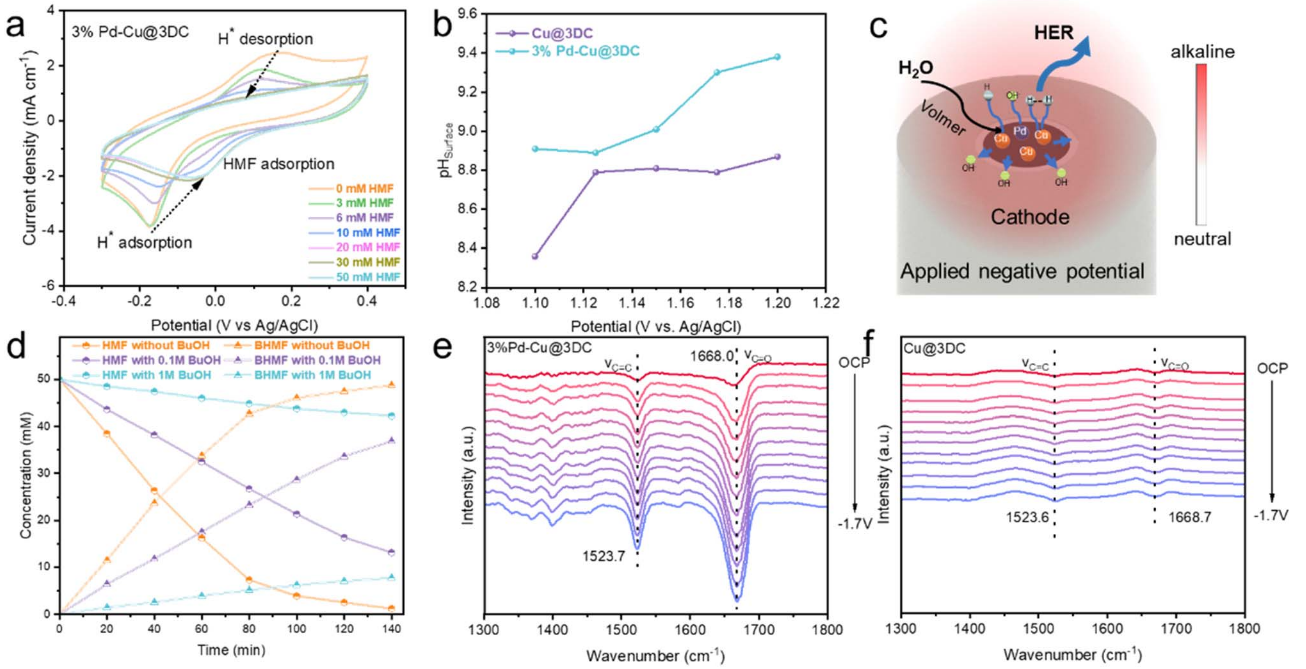

Fig. 4 Electrocatalytic reaction mechanism analysis. (a) CV curves of 3%Pd-Cu@3DC in 0.5 M $KHCO_3$ with different HMF concentrations. (b) Local pH values on the surface of 3%Pd-Cu@3DC and Cu@3DC at varied potentials. (c) Schematic illustration of the OH^- enrichment effect on 3%Pd-Cu@3DC for electrochemical HMF hydrogenation. (d) *t*-BuOH scavenging of H* species. (e and f) *In situ* ATR-SEIRAS spectroscopy recorded for (e) 3%Pd-Cu@3DC and (f) Cu@3DC.

reflecting sluggish OH^- production. This pH gradient difference provides direct mechanistic evidence for the enhanced H* availability on Pd-Cu@3DC, where atomic Pd sites facilitate water dissociation ($H_2O + e^- \rightarrow H^* + OH^-$) (Fig. 4c). The synergistic effect creates a self-sustaining alkaline microenvironment that accelerates HMF → BHMF conversion kinetics while suppressing competitive H_2 evolution through localized OH^- accumulation.

In order to further validate the supposition, *tert*-butyl alcohol (*t*-BuOH) was used to scavenge the H* species.[42] As shown in Fig. 4d, a notably decreased HMF-to-BHMF conversion can be found after *t*-BuOH was introduced into the system, because H* was partly consumed by *t*-BuOH rather than reacting with HMF. This indicates that the H* generated through the Volmer step plays an essential role in the electrochemical hydrogenation of HMF.[37] To further explore the reaction mechanism, we investigated the dependence of the reaction rate on HMF concentration. According to the work by Lopez-Ruiz,[43] the reduction of HMF *via* the ECH process, HMF hydrogenation subsequent to H* formation—follows the Langmuir–Hinshelwood (L–H) mechanism, which is indicative of competitive adsorption between HMF and H_2O. Consequently, a negative reaction order with respect to HMF is anticipated at higher concentrations. As depicted in Fig. S10, a negative reaction order was observed over the catalyst with increasing HMF concentration. This observation, consistent with the *t*-BuOH H* species scavenging experiment, collectively confirms that the reaction indeed adheres to the Langmuir–Hinshelwood (L–H) mechanism. Then, the reaction energetics were modeled under *operando* neutral conditions (0.5 M $KHCO_3$, pH = 8.17), where the L–H mechanism dominates through surface-adsorbed hydrogen (H*) intermediates.[44]

Density functional theory (DFT) calculations were systematically performed to elucidate the atomic-scale mechanism governing HMF hydrogenation and competing hydrogen evolution reaction (HER) pathways on Pd-Cu@3DC. Surface slab models of Cu(111) and Pd-doped Cu(111) surfaces were constructed based on the experimental results, and the Gibbs free energies of H* (ΔG_{H^*}) and HMF* adsorption (ΔG_{HMF^*}) were also calculated. The pristine Cu(111) surface exhibits a ΔG_{H^*} value of −3.53 eV on the Cu sites, which suggests weak affinity for the H* atom. Interestingly, the Cu site near the Pd atom of the Pd–Cu model exhibits a relatively lower ΔG_{H^*} of −3.58 eV, demonstrating the crucial role of Pd doping in affording Cu active sites for H* adsorption (Fig. 5a). It is noteworthy that the catalyst must facilitate the activation and dissociation of H_2O to produce adsorbed H* species on its surface during the L–H mechanism. Therefore, we also assess the free energy change during the formation of OH^- and H* from H_2O. As shown in Fig. 5b, the calculated energy barrier for each step of H_2O conversion to OH^- and H* on the Pd–Cu model (1.23 eV) is lower than that on the Cu model (1.54 eV).

Generally, the changes in open circuit potential (OCP) reflect the HMF adsorption ability on the catalyst surface.[45] As depicted in Fig. 5c, as the Pd doping content increases, the magnitude of the OCP elevation following the introduction of 50 mM HMF also increases. For Pd@3DC, the OCP increases by 0.1338 V after HMF introduction, which is approximately five times that of Cu@3DC (0.0266 V), demonstrating that Pd exhibits a specific affinity for HMF adsorption. In addition, the calculated ΔG_{HMF^*}(Fig. 5d) results suggest that HMF prefers to adsorb on the Pd site with a ΔG_{HMF^*} of −0.85 eV, while it is weakly adsorbed on Cu (−0.68 eV). The longer C═O bond length (1.25 Å) of HMF molecules on the surface of Pd–Cu than on Cu (1.24 Å) also indicates that Pd–Cu exhibits a stronger activation effect toward HMF. The potential-dependent *in situ* ATR-SEIRAS spectra of 3%Pd-Cu@3DC (Fig. 4e and f) exhibit an intensified C═O stretching band at 1668 cm^{-1} and a stronger C═C stretching band at 1523 cm^{-1} compared to Cu@3DC, which demonstrates the strong adsorption of HMF on the catalyst surface.[46] Fig. 5e shows the optimized free energies of the hydrogenation pathway from HMF to BHMF on both model surfaces. It is evident that the hydrogenation of HMF is an energy uphill process with a ΔG of 0.79 eV for Pd–Cu, which is smaller than that of Cu (0.90 eV). The results imply that HMF hydrogenation could be energetically more favored on Pd–Cu, further revealing the crucial role of Pd doping. Pd exhibits a much stronger adsorption affinity for HMF than Cu. However, poor product desorption may compromise its HMF hydrogenation efficiency (Fig. S4c). In contrast, pure Cu exhibits inferior water dissociation capability, failing to generate sufficient H* species and thus rendering HMF hydrogenation inefficient ((Fig. S4a). Thus, we propose that in the present system, Pd sites generate H* *via* the Volmer step, while synergizing with Cu to adsorb HMF molecules, thereby accelerating the hydrogenation process.

Therefore, a reaction mechanism is proposed herein (Fig. 5f). Initially, a H_2O molecule is acquired to adsorb on the electrode. Driven by electrons and the active sites, H_2O was split to generate H*. Meanwhile, HMF is adsorbed on the Pd site to form HMF*, and the –CH═O was activated. Subsequently, the HMF hydrogenation process proceeds *via* initial hydrogenation on the C site and subsequently on the O site in the aldehyde group.[44,47] Additionally, the HER is discerned as the main competing reaction in this process, due to the coupling of H* to form H_2. Consequently, it is crucial to optimize the reaction conditions and achieve a balance between the HMF hydrogenation reaction and the HER by adjusting parameters such as the HMF concentration, electrolytic potential, and even the catalyst materials.

BHMF production and application

Considering the superior performance of 3%Pd-Cu@3DC, we further explored its successive production capability for the HMF electrochemical hydrogenation by applying a proton exchange membrane (PEM)-based flow reactor. As shown in Fig. S14, a photograph of the PEM flow reactor for the continuous electroreduction of HMF to BHMF is presented. HMF solution is fed into the cathodic chamber, transported to the catalyst surface and electrochemically reduced to the targeted BHMF (Fig. 6a). As shown in Fig. 6b, the conversion and FE increase as the applied potential increased from −1.6 to −2.4 V. When the potential was increased to −2.4 V, a maximum BHMF

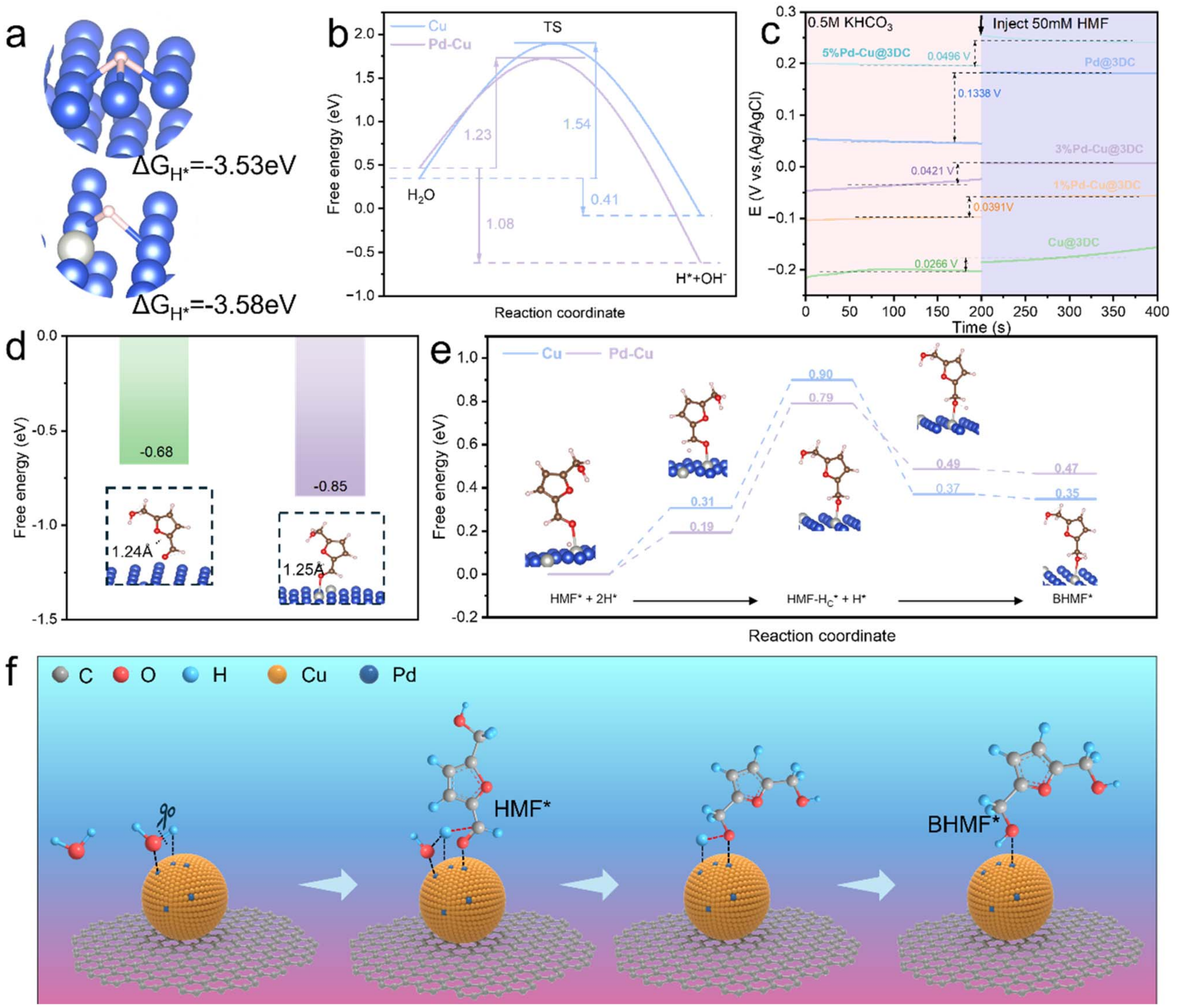

Fig. 5 DFT theoretical calculations for the reaction pathway and mechanism on Pd–Cu and Cu for HMF hydrogenation to BHMF. (a) Adsorption free energy (ΔG_{H*}) of H* and (b) the calculated ΔG for water splitting to produce an adsorbed H* species on Pd–Cu and Cu. (c) OCP curves of Cu@3DC, 1%Pd-Cu@3DC, 3%Pd-Cu@3DC, 5%Pd-Cu@3DC and Pd@3DC in 0.5 M $KHCO_3$ solution and 0.5 M $KHCO_3$ + 50 mm HMF solution. (d) Adsorption free energy (ΔG_{HMF*}) of HMF and (e) the calculated ΔG for HMF hydrogenation to BHMF on Pd–Cu and Cu. (f) Proposed mechanism of HMF electrochemical reduction on 3%Pd-Cu@3DC.

conversion of 91% was achieved, with a current of −60 mA and an FE of 99%. Once the potential continues to increase, FE will decrease due to the competing HER. The stability was also preliminarily evaluated at −2.4 V, retaining an FE of above 95% and a conversion of 90% during 12 h of electrolysis (Fig. 6c). The BHMF was obtained from the effluent by an evaporation crystallization–extraction–evaporation crystallization strategy (Fig. S8). As shown in Fig. S8, the obtained product is similar to the BHMF purchased from Aladdin, with a purity of 99%.

Next, to assess the techno-economic viability of successive production for electrocatalytic conversion of HMF into BHMF, we proposed an integrated process model, encompassing an electrolyzer and evaporation crystallization and extraction systems (Fig. 6d). The model aligned operating parameters with experimental results from the PEM electrolyzer. The system produces 1 ton (t) per day of BHMF using 1.16 t per day HMF. As shown in subdivided cost evaluation (Fig. 6e), BHMF can be produced at the cost of $626.4 per t *via* the cascade process. Among the costs, separation equipment accounts for 17.5%, followed by electrolyzer (16.7%) and catalyst-membrane costs (16.5%). In addition, economic analysis showed a 20-year net present value (NPV) of $40 million and a 2-year payout period (Fig. 6f). These results reveal that using renewable energy for electrocatalytic HMF hydrogenation to prepare BHMF possesses high economic feasibility.

Finally, we demonstrated the downstream application of BHMF as a versatile building block for producing bio-based polyester. Poly(2,5-furandimethylene succinate) (PFS) was synthesized by solution condensation polymerization between BHMF and succinic acid (Fig. 6g). GPC results confirmed that

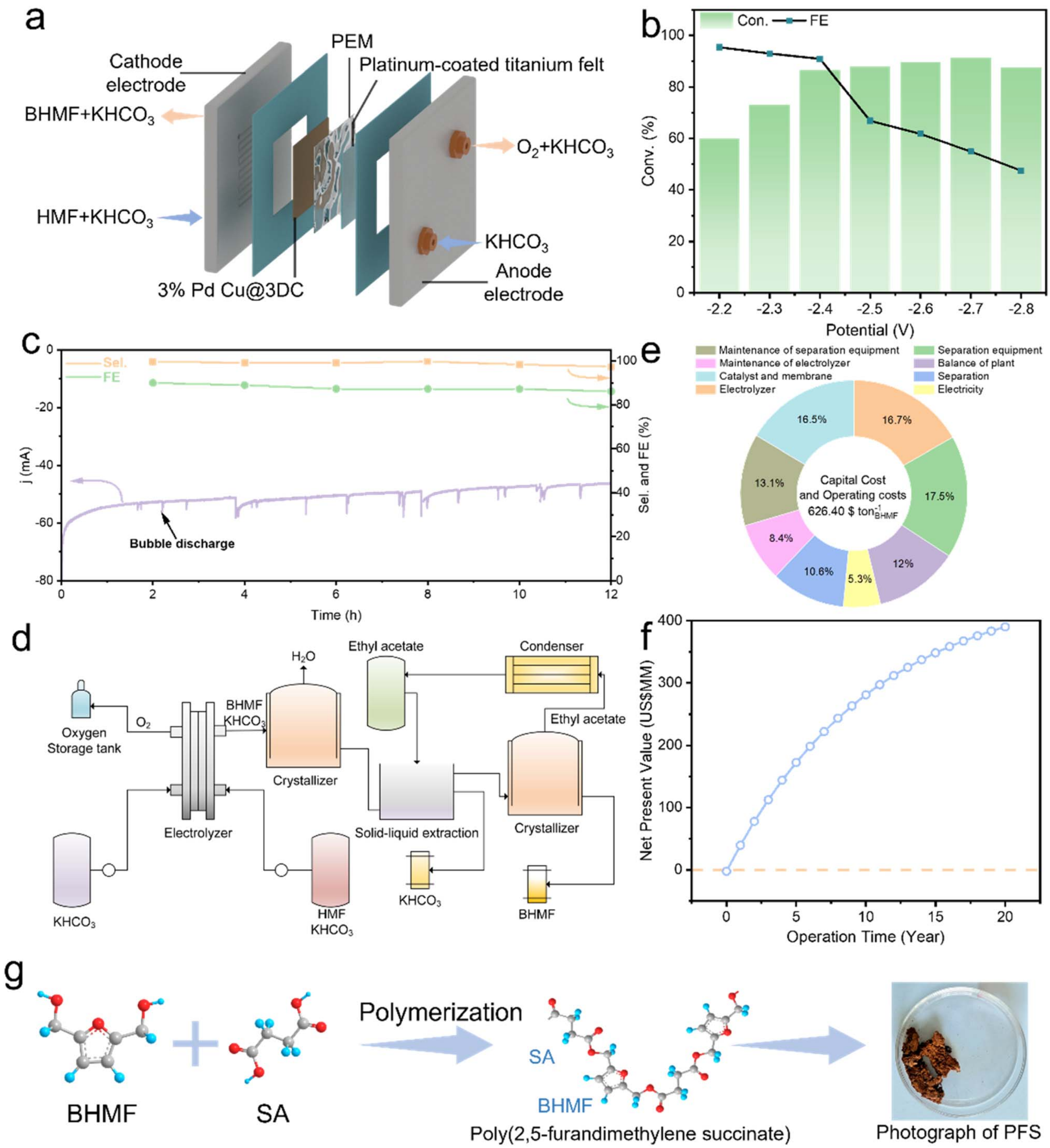

Fig. 6 (a) Schematic illustration of a PEM electrolyzer. (b) HMF conversion at different potentials. (c) Selectivity and FE of BHMF during the chronoamperometry test. (d) Integrated process model for BHMF production. (e) Proportion of expenses in each part of the production process. (f) NPV curve over 20 years. (g) BHMF polymerization with SA to produce PFS.

the molecular weight (M_n) of the obtained PFS was ~10 861 and the polydispersity was 1.78 (Fig. S9a and Table S1). Additionally, DSC analysis illustrates that the obtained PFS exhibits a T_g (glass transition temperature) of 50.6 °C and a T_m (melting onset temperature) of 85.2 °C (Fig. S9b). These characteristics illustrate the high potential of the renewable PFS to play a role in a sustainable and circular plastic market.

Conclusion

In summary, novel Pd-Cu@3DC catalysts were constructed by a salt template space-confined strategy. The unique atomic-level doping with internal charge transfer provides sites for enhanced adsorption and activation of H_2O molecules to facilitate H* generation. Interestingly, the obtained Pd-Cu@3DC catalyst exhibits high BHMF selectivity and FE of 99.3% and 97.5%, respectively, at −1.15 V (*vs.* Ag/AgCl), and remains stable for 13 cycles without obvious decay. The mechanistic study reveals that Pd doping enhances the adsorption of H* and HMF* and promotes the hydrogenation steps by lowering the energy barrier of the crucial step. These results describe a novel method for further applications while providing an in-depth understanding of dopant engineering in electrocatalysts to regulate electrocatalytic activity and selectivity.

Author contributions

G. F.: investigation, data collection; Y. F.: software, validation; L. D.: methodology, writing – review & editing, funding acquisition; Z. M.: funding acquisition; J. Z.: supervision.

Conflicts of interest

There are no conflicts to declare.

Data availability

All the data supporting this article have been included in the main text and the supplementary information (SI). Supplementary information: materials and methods and supplementary data. See DOI: https://doi.org/10.1039/d5sc06257h.

Acknowledgements

This work was supported by the National Natural Science Foundation of China, China (grant number 52101263) and the Shandong Provincial Natural Science Foundation, China (grant numbers ZR2021QE231 and ZR2020QB048).

Notes and references

1 B. Hu, Q. Lu, X. Jiang, X. Dong, M. Cui, C. Dong and Y. Yang, Pyrolysis mechanism of glucose and mannose: The formation of 5-hydroxymethyl furfural and furfural, *J. Energy Chem.*, 2018, **27**(2), 486–501, DOI: 10.1016/j.jechem.2017.11.013.

2 Z. Li, J. Sun, Y. Wang, Y. Song, J. Yang, X. Liu and L. Zhang, Construction of CoO–Cu_2O Composites With Enhanced HMF Adsorption and Passivated Water Oxidation for High-Efficiency Biomass Valorization, *ACS Sustain. Chem. Eng.*, 2025, **13**(15), 5645–5654, DOI: 10.1021/acssuschemeng.5c00177.

3 Q. Hou, X. Qi, M. Zhen, H. Qian, Y. Nie, C. Bai, S. Zhang, X. Bai and M. Ju, Biorefinery Roadmap Based on Catalytic Production and Upgrading 5-Hydroxymethylfurfural, *Green Chem.*, 2021, **23**(1), 119–231, DOI: 10.1039/d0gc02770g.

4 P. Zhu, M. Shi, Z. Shen, X. Liao and Y. Chen, Electrocatalytic Conversion of Biomass-Derived Furan Compounds: Mechanisms, Catalysts and Perspectives, *Chem. Sci.*, 2024, **15**(13), 4723–4756, DOI: 10.1039/d4sc00546e.

5 C. Xu, E. Paone, D. Rodríguez-Padrón, R. Luque and F. Mauriello, Recent catalytic routes for the preparation and the upgrading of biomass derived furfural and 5-hydroxymethylfurfural, *Chem. Soc. Rev.*, 2020, **49**(13), 4273–4306, DOI: 10.1039/d0cs00041h.

6 G.-H. Wang, J. Hilgert, F. H. Richter, F. Wang, H.-J. Bongard, B. Spliethoff, C. Weidenthaler and F. Schüth, Platinum–cobalt bimetallic nanoparticles in hollow carbon nanospheres for hydrogenolysis of 5-hydroxymethylfurfural, *Nat. Mater.*, 2014, **13**(3), 293–300, DOI: 10.1038/nmat3872.

7 S. Wang and G. Song, A pathway to bio-based aromatics, *Nat Sustainability*, 2023, **6**(11), 1295–1296, DOI: 10.1038/s41893-023-01191-9.

8 J. Zhang, H. Qin, X. Cao, W. Jia, R. Ma, X. Chen, W. Xia, G. Lin and L. Jiao, Constructing Adjustable Heterointerface for Enhancing Acidic Oxygen Evolution Performances of RuO_2@$CoMnO_3$ Nanosheets Electrocatalysts, *ACS Mater. Lett.*, 2024, **6**(7), 3016–3024, DOI: 10.1021/acsmaterialslett.4c00778.

9 Y. F. Guo, L. Yang, L. Z. Zhang, S. Chen, L. J. Sun, S. J. Gu and Z. W. You, A Dynamically Hybrid Crosslinked Elastomer for Room-Temperature Recyclable Flexible Electronic Devices, *Adv. Funct. Mater.*, 2021, **31**(50), 2106281, DOI: 10.1002/adfm.202106281.

10 G. Ratrey, B. S. Solanki, S. P. Kamble and C. V. Rode, Highly Efficient Chemoselective Hydrogenation of 5-HMF to BHMF over Reusable Bimetallic Pd-Ir/C Catalyst, *ChemistrySelect*, 2022, **7**(23), e202200456, DOI: 10.1002/slct.202200456.

11 B. Kang, Z. Chen, J. Yang, M. Lv, H. He, G. Chen, L. Huai, C. Chen and J. Zhang, Boosting Hydrogenation Properties of Supported Cu-Based Catalysts by Replacing Cu_0 Active Sites, *Appl. Catal., B*, 2025, **361**, 124563, DOI: 10.1016/j.apcatb.2024.124563.

12 Y. Kwon, K. J. P. Schouten, J. C. van der Waal, E. de Jong and M. T. M. Koper, Electrocatalytic Conversion of Furanic Compounds, *ACS Catal.*, 2016, **6**(10), 6704–6717, DOI: 10.1021/acscatal.6b01861.

13 X. Linghu, J. Chen, L. Jiang and T. Wang, Recent progress in bismuth-based materials for electrochemical CO_2 reduction to formate/formic acid, *Nano Mater. Sci.*, 2024, DOI: 10.1016/j.nanoms.2024.11.007.

14 T. Ali, H. Wang, W. Iqbal, T. Bashir, R. Shah and Y. Hu, Electro-Synthesis of Organic Compounds with Heterogeneous Catalysis, *Adv. Sci.*, 2022, **10**(1), 2205077, DOI: 10.1002/advs.202205077.

15 F. M. Yap, G. Z. Sheng Ling, B. J. Su, J. Y. Loh and W.-J. Ong, Recent advances in structural modification on graphitic carbon nitride (g-C_3N_4)-based photocatalysts for high-efficiency photocatalytic H_2O_2 production, *Nano Res. Energy*, 2024, **3**(1), 1–51, DOI: 10.26599/nre.2023.9120091.

16 X. H. Chadderdon, D. J. Chadderdon, J. E. Matthiesen, Y. Qiu, J. M. Carraher, J. P. Tessonnier and W. Li, Mechanisms of Furfural Reduction on Metal Electrodes: Distinguishing Pathways for Selective Hydrogenation of Bioderived Oxygenates, *J. Am. Chem. Soc.*, 2017, **139**(40), 14120–14128, DOI: 10.1021/jacs.7b06331.

17 B. Zhu, J. Yang, Q. Wang, X. Yu, S. Fan, W. Xie, J. Zhang and C. Chen, Corrosion-Induced CoCu Microwire Arrays for

Efficient Electroreduction of 5-Hydroxymethylfurfural, *Chem Catal.*, 2025, **5**(4), 101259, DOI: 10.1016/j.checat.2024.101259.

18 Y.-R. Zhang, B.-X. Wang, L. Qin, Q. Li and Y.-M. Fan, A non-noble bimetallic alloy in the highly selective electrochemical synthesis of the biofuel 2,5-dimethylfuran from 5-hydroxymethylfurfural, *Green Chem.*, 2019, **21**(5), 1108–1113, DOI: 10.1039/c8gc03689f.

19 A. Ciotti, M. Rahaman, C. W. S. Yeung, T. Li, E. Reisner and M. García-Melchor, Driving Electrochemical Organic Hydrogenations on Metal Catalysts by Tailoring Hydrogen Surface Coverages, *J. Am. Chem. Soc.*, 2025, **147**(16), 13158–13168, DOI: 10.1021/jacs.4c15821.

20 S. Li, Z. Kan, J. Bai, A. Ma, J. Lu and S. Liu, Rational Design of Transition-Metal-Based Catalysts for the Electrochemical 5-Hydroxymethylfurfural Reduction Reaction, *ChemSusChem*, 2024, **17**(24), e202400869, DOI: 10.1002/cssc.202400869.

21 C. Tian, J. Q. Yu, D. J. Zhou, H. J. Ze, H. Z. Liu, Y. J. Chen, R. Xia, P. F. Ou, W. Y. Ni, K. Xie, *et al.*, Reduction of 5-Hydroxymethylfurfural to 2,5-Bis(hydroxymethyl)Furan at High Current Density using a Ga-Doped AgCu:Cationomer Hybrid Electrocatalyst, *Adv. Mater.*, 2024, **36**(24), 2312778, DOI: 10.1002/adma.202312778.

22 X. Cao, Y. Ding, D. Chen, W. Ye, W. Yang and L. Sun, Cluster-Level Heterostructure of PMo12/Cu for Efficient and Selective Electrocatalytic Hydrogenation of High-Concentration 5-Hydroxymethylfurfural, *J. Am. Chem. Soc.*, 2024, **146**(36), 25125–25136, DOI: 10.1021/jacs.4c08205.

23 W. Zhang, W. Ge, Y. Qi, X. Sheng, H. Jiang and C. Li, Surfactant Directionally Assembled at the Electrode-Electrolyte Interface for Facilitating Electrocatalytic Aldehyde Hydrogenation, *Angew. Chem., Int. Ed.*, 2024, **63**(31), e202407121, DOI: 10.1002/anie.202407121.

24 P. Hauke, T. Merzdorf, M. Klingenhof and P. Strasser, Hydrogenation Versus Hydrogenolysis during Alkaline Electrochemical Valorization of 5-Hydroxymethylfurfural Over Oxide-Derived Cu-Bimetallics, *Nat. Commun.*, 2023, **14**(1), 4708, DOI: 10.1038/s41467-023-40463-y.

25 Z. Zhao, R. Yu, S. Wang, L. Guo, L. Zhang, M. Chen, J. Chen and H. Zheng, Introducing Fe into Cu-Based Catalyst to Boost The Electrocatalytic Hydrogenation of 5-Hydroxymethylfurfural, *ChemSusChem*, 2025, **18**(1), e202401278, DOI: 10.1002/cssc.202401278.

26 R. Guo, Y. Zeng, L. Lin, D. Hu, C. Lu, S. Conroy, S. Zhang, C. Zeng, H. Luo, Z. Jiang, *et al.*, CO_2-Assisted Controllable Synthesis of PdNi Nanoalloys for Highly Selective Hydrogenation of Biomass-Derived 5-Hydroxymethylfurfural, *Angew. Chem., Int. Ed.*, 2024, **64**(6), e202418234, DOI: 10.1002/anie.202418234.

27 B. Boro, P. Koley, A. Boruah, T. Hosseinnejad, J. M. Lee, C.-C. Chang, C.-W. Pao, S. Bhargava and J. Mondal, Deciphering Reactivity Factors of Cu(II)–Pd(0) Engaged in Porous Organic Polymer toward Catalytic Hydrogenolysis of 5-Hydroxymethylfurfural to 2,5-Dimethylfuran, *ACS Sustain. Chem. Eng.*, 2024, **12**(38), 14200–14217, DOI: 10.1021/acssuschemeng.4c04337.

28 K. Cui, T. Wang, Q. Zhang and H. Zhang, Multi-Functional Descriptor Design of V-Based Double Atomic Catalysts for Room Temperature Sodium-Sulfur Batteries, *Small*, 2024, **21**(4), 2409866, DOI: 10.1002/smll.202409866.

29 L. Diao, B. Zhang, Q. Sun, N. Wang, N. Zhao, C. Shi, E. Liu and C. He, An in-plane Co_9S_8@MoS_2 heterostructure for the hydrogen evolution reaction in alkaline media, *Nanoscale*, 2019, **11**(44), 21479–21486, DOI: 10.1039/c9nr06609h.

30 Y. Deng, J. Wang, S.-F. Zhang, Z.-J. Zhang, J.-F. Sun, T.-T. Li, J.-L. Kang, H. Liu and S. Bai, In Situ Constructing Lamella-Heterostructured Nanoporous CoFe/$CoFe_2O_4$ and CeO_{2-x} as Bifunctional Electrocatalyst for High-Current-Density Water Splitting, *Rare Metals*, 2024, **44**(2), 1053–1066, DOI: 10.1007/s12598-024-02926-z.

31 L. Li, P. Wang, Q. Shao and X. Huang, Metallic nanostructures with low dimensionality for electrochemical water splitting, *Chem. Soc. Rev.*, 2020, **49**(10), 3072–3106, DOI: 10.1039/d0cs00013b.

32 W. Jiang, J. K. Liu, H. Zhou, Z. J. Huang, Y. X. Wu, S. Cao, D. X. Yang, X. L. Wang, P. F. Liu and Y. Zhou, Operando *OH Tracking Unveils Heteroatom-Tailored Co_3O_4 Spinel Catalyst for Industrial-Level Current Density Ethylene Glycol Electrooxidation, *ACS Catal.*, 2025, **15**(21), 18612–18622, DOI: 10.1021/acscatal.5c06358.

33 M. Zheng, P. Wang, Y. Gao, C. Peng, Y. Zheng and S.-Z. Qiao, Tuning interfacial *H coverage and aldehyde adsorption configuration for selective electrocatalytic hydrogenation of furfural, *J. Mater. Chem. A*, 2025, **13**(13), 9135–9143, DOI: 10.1039/d5ta00403a.

34 M. G. Sendeku, K. Harrath, F. T. Dajan, B. Wu, S. Hussain, N. Gao, X. Zhan, Y. Yang, Z. Wang, C. Chen, *et al.*, Deciphering In-situ Surface Reconstruction in Two-Dimensional CdPS3 Nanosheets for Efficient Biomass Hydrogenation, *Nat. Commun.*, 2024, **15**(1), 5174, DOI: 10.1038/s41467-024-49510-8.

35 L. Peng, Y. Yu, S. Gao, M. Wang, J. Zhang, R. Zhang, W. Jia, Y. Sun and H. Liu, Coupling Cu+ Species and Zr Single Atoms for Synergetic Catalytic Transfer Hydrodeoxygenation of 5-Hydroxymethylfurfural, *ACS Catal.*, 2024, **14**(9), 6623–6632, DOI: 10.1021/acscatal.4c00763.

36 A. R. Zeradjanin, P. Narangoda, J. Masa and R. Schlögl, What Controls Activity Trends of Electrocatalytic Hydrogen Evolution Reaction?─Activation Energy Versus Frequency Factor, *ACS Catal.*, 2022, **12**(19), 11597–11605, DOI: 10.1021/acscatal.2c02964.

37 H. Xu, G. Xu, B. Huang, J. Yan, M. Wang, L. Chen and J. Shi, Zn-Organic Batteries for the Semi-Hydrogenation of Biomass Aldehyde Derivatives and Concurrently Enhanced Power Output, *Angew. Chem., Int. Ed.*, 2023, **62**(20), e202218603, DOI: 10.1002/anie.202218603.

38 H. Wen, Z. Fan, S. Dou, J. C.-H. Lam, W. Zhang and Z. Chen, Electrochemical hydrogenation of furfural under alkaline conditions with enhanced furfuryl alcohol selectivity by self-grown Cu on a Ag electrode, *Inorg. Chem. Front.*, 2024, **11**(14), 4449–4458, DOI: 10.1039/d4qi00763h.

39 K. Ji, M. Xu, S. M. Xu, Y. Wang, R. Ge, X. Hu, X. Sun and H. Duan, Electrocatalytic Hydrogenation of 5-Hydroxymethylfurfural Promoted by a Ru_1Cu Single-Atom Alloy Catalyst, *Angew. Chem., Int. Ed.*, 2022, **61**(37), e202209849, DOI: 10.1002/anie.202209849.

40 X. Zheng, X. Shi, H. Ning, R. Yang, B. Lu, Q. Luo, S. Mao, L. Xi and Y. Wang, Tailoring a Local Acid-like Microenvironment for Efficient Neutral Hydrogen Evolution, *Nat. Commun.*, 2023, **14**(1), 4209, DOI: 10.1038/s41467-023-39963-8.

41 B. Huang, J. Yan, Z. Li, L. Chen and J. Shi, Anode-Electrolyte Interfacial Acidity Regulation Enhances Electrocatalytic Performances of Alcohol Oxidations, *Angew. Chem., Int. Ed.*, 2024, **63**(40), e202409419, DOI: 10.1002/anie.202409419.

42 S. Tang, N. Guo, C. Chen, B. Yao, X. Liu, C. Ma, Q. Liu, S. Ren, C. He, B. Liu, *et al.*, Electrochemical Alkyne Semi-Hydrogenation via Proton-Coupled Electron Transfer on Cu(111) Surface, *Angew. Chem., Int. Ed.*, 2025, **137**(37), e202510192, DOI: 10.1002/anie.202510192.

43 J. A. Lopez-Ruiz, U. Sanyal, J. Egbert, O. Y. Gutiérrez and J. Holladay, Kinetic Investigation of the Sustainable Electrocatalytic Hydrogenation of Benzaldehyde on Pd/C: Effect of Electrolyte Composition and Half-Cell Potentials, *ACS Sustain. Chem. Eng.*, 2018, **6**(12), 16073–16085, DOI: 10.1021/acssuschemeng.8b02637.

44 M. G. Sendeku, K. Harrath, F. T. Dajan, B. Wu, S. Hussain, N. Gao, X. Zhan, Y. Yang, Z. Wang, C. Chen, *et al.*, Deciphering in-situ surface reconstruction in two-dimensional CdPS3 nanosheets for efficient biomass hydrogenation, *Nat. Commun.*, 2024, **15**(1), 5174, DOI: 10.1038/s41467-024-49510-8.

45 Y. Chen, J. Qiu, S. Li, J. Zhang, Y. Liu, X. Chen, X. Liu, S. Dou and D. Wang, Spontaneous Corrosion Induced Scalable Fabrication of Bayberry-Like Ni@Ni3S2 Core–Shell Catalysts for 5-Hydroxymethylfurfural Oxidation, *Adv. Funct. Mater.*, 2024, **35**(5), 2414587, DOI: 10.1002/adfm.202414587.

46 Y. Wu, Y. Jiang, W. Chen, X. Yue, C. L. Dong, M. Qiu, T. T. T. Nga, M. Yang, Z. Xia, C. Xie, *et al.*, Selective Electroreduction of 5-Hydroxymethylfurfural to Dimethylfuran in Neutral Electrolytes via Hydrogen Spillover and Adsorption Configuration Adjustment, *Adv. Mater.*, 2023, **36**(7), 2307799, DOI: 10.1002/adma.202307799.

47 X. Guo, H. Fu, J. Yang, L. Luo, H. Zhou, M. Xu, X. Kong, M. Shao, H. Duan and Z. Li, Promoting Electrocatalytic Hydrogenation of 5-Hydroxymethylfurfural over a Cooperative Ag/SnO_2 Catalyst in a Wide Potential Window, *ACS Catal.*, 2023, **13**(20), 13528–13539, DOI: 10.1021/acscatal.3c03005.